PHYSICAL REVIEW MATERIALS **6**, 094418 (2022)

Editors' Suggestion

Probing antiferromagnetic coupling in magnetic insulator/metal heterostructures

Patrick Quarterman,[1,*] Yabin Fan,[2] Zhijie Chen,[3] Christopher J. Jensen,[3] Rajesh V. Chopdekar,[4] Dustin A. Gilbert,[5] Megan E. Holtz,[6,7] Mark D. Stiles,[8] Julie A. Borchers,[1] Kai Liu,[3] Luqiao Liu,[2] and Alexander J. Grutter[1,†]

[1]*NIST Center for Neutron Research, National Institute of Standards and Technology, 100 Bureau Dr., Gaithersburg, Maryland 20899, USA*
[2]*Microsystems Technology Laboratories, Massachusetts Institute of Technology, Cambridge, Massachusetts 02139, USA*
[3]*Physics Department, Georgetown University, Washington, DC 20057, USA*
[4]*Advanced Light Source, Lawrence Berkeley National Laboratory, Berkeley, California 94720, USA*
[5]*Department of Materials Science and Engineering, University of Tennessee, Knoxville, Tennessee 37996, USA*
[6]*Materials Measurement Laboratory, National Institute of Standards and Technology, 100 Bureau Dr., Gaithersburg, Maryland 20899, USA*
[7]*Department of Metallurgical and Materials Engineering, Colorado School of Mines, Golden, Colorado 80401, USA*
[8]*Center for Nanoscale Science and Technology, National Institute of Standards and Technology,*
100 Bureau Dr., Gaithersburg, Maryland 20899, USA

(Received 4 May 2022; revised 24 June 2022; accepted 31 August 2022; published 30 September 2022)

Using depth- and element-resolved characterization, we report insights into antiferromagnetic coupling in $Y_3Fe_5O_{12}$/permalloy (YIG/Py) and $Y_3Fe_5O_{12}$/Co (YIG/Co) thin-film heterostructures grown on Si/SiO_2 and $Gd_3Ga_5O_{12}$ substrates. We build on recent work demonstrating antiferromagnetic coupling in polycrystalline YIG/metallic-ferromagnetic systems by characterizing differences in the structural and magnetic properties which depend on the choice of ferromagnet (Py vs Co), seed layer (with and without Pt), and substrate (Si/SiO_2 vs $Gd_3Ga_5O_{12}$). These differences in the sample structure manifest as notable changes in interface coupling sign, magnetic reversal mechanisms, magnetic depth profiles, and domain structure. Through a combination of magnetometry, polarized neutron reflectometry, and x-ray photoemission electron microscopy, a comprehensive picture of the magnetic interactions is realized, with lateral- and depth resolution at submicrometer and nanometer scales, respectively. These results confirm that both Co and Py share a preference to align antiparallel to polycrystalline YIG grown on some substrates (Si/SiO_2 and Si/SiO_2/Pt), while coupling ferromagnetically with highly oriented YIG on (111) $Gd_3Ga_5O_{12}$ and (110) $Gd_3Ga_5O_{12}$/Pt substrates. The complex interplay among magnetic interactions at the YIG/ferromagnetic interface has important implications for spintronic and magnonic devices based on this platform.

DOI: 10.1103/PhysRevMaterials.6.094418

I. INTRODUCTION

Heterostructures consisting of magnetic insulators and ferromagnetic metals are of wide interest as platforms for magnon physics and applications in nonvolatile memories [1]. Yttrium-iron-garnet ($Y_3Fe_5O_{12}$, YIG) is an extensively studied ferrimagnetic insulator with a low Gilbert damping constant [2] and long spin-wave propagation lifetime [3,4], which make it an important candidate for use in domain-wall memories [5] and magnon spintronics [6,7]. In the context of magnon studies, YIG is capable of hosting standing spin waves (SSW) and interlayer magnon-magnon coupling when in proximity to a soft ferromagnetic metal [8–10]. YIG-based spin-wave structures are also exciting for enabling quantum functionalities [11–13]. The interlayer exchange interaction in YIG/metal ferromagnetic (FM) systems has been demonstrated to exhibit the magnon spin-valve effect [14,15]. Magnon spin valves are potentially advantageous compared to traditional magnetic memories, as transmitting information through pure spin currents rather than a spin-polarized current dramatically reduces the associated Joule heating, improving their energy efficiency [6].

YIG films used for fundamental research are typically grown epitaxially on $Gd_3Ga_5O_{12}$ (GGG) substrates. However, GGG is not compatible with complementary metal-oxide semiconductor (CMOS)-based heterostructures, limiting the technological relevance of these systems. In addition, there have been numerous reports of interdiffusion between YIG thin films and GGG substrates, leading to complex magnetic interactions which vary from sample to sample and degrade device performance [16,17]. While the development of YIG/FM hybrid structures on Si/SiO_2 substrates would yield significant advantages, the exploration of such systems remains in its infancy and much of the associated materials physics is poorly understood. For example, we have recently reported intrinsic antiparallel coupling in sputtered Si/SiO_2/Pt/YIG/permalloy ($Ni_{80}Fe_{20}$, Py) heterostructures with a coupling field as large as 150 mT [18]. That work demonstrated that the coupling is due to an interfacial exchange interaction rather than dipole interactions, and that the magnetization reversal process can be tuned by changing the ratio of the YIG and Py magnetic moments through

---

[*] patrick.quarterman@gmail.com
[†] alexander.grutter@nist.gov

their respective layer thicknesses. Furthermore, we have used the antiparallel coupling in this Si-based heterostructure to fabricate a magnon spin valve with an ON/OFF ratio of 130% at room temperature. However, much remains unknown about this unexpected magnetic configuration, particularly the underlying source of this antiparallel exchange interaction and its applicability to other FM layers or substrates.

Here we note the work of Klingler *et al.,* which suggested a comparable magnetic configuration in a YIG/Co heterostructure with a very different geometry [8]. In that study, the authors interrogated specially prepared 1-μm YIG films grown on (111)-oriented GGG substrates by liquid phase epitaxy and capped with 35 to 50 nm of Co, proposing an antiparallel configuration with a vertical domain wall in the YIG layer. The YIG surface in Klingler *et al.* was prepared through etching and *in situ* annealing prior to Co deposition.

When considered in tandem, these observations of antiparallel alignment of YIG and FM [8,18] suggest that the interface coupling is determined by a complex interplay among a number of factors. For example, surface termination and interface chemistry may play a critical role, depending on whether the dominant coupling mechanism is direct exchange or oxygen-mediated superexchange between Fe in the YIG and Fe/Co/Ni in the adjacent metal. If the interfacial metal forms surface bonds with YIG oxygen, the sign of the resulting exchange will depend on unknown ferromagnetic metal valence states at the surface as well as bond angles across the interface, all of which vary with surface termination. It may therefore be expected that Fe^{2+}-O-Fe superexchange may yield a different exchange coupling sign than, for example, Fe^{3+}-O-Co superexchange or Fe^{2+}-Ni direct exchange. Magnetic disorder and frustration at a polycrystalline YIG surface may also play a role. Lastly, we note that the growth of iron garnet systems is a notoriously temperamental process, and any unexpected outcomes such as antiparallel coupling must be carefully assessed to ensure they do not arise from sample quality issues induced by a specific growth process such as the dc magnetron sputtering used in Ref. [18].

Unfortunately, the complexity of a polycrystalline metal-oxide interface with multiple valence states and an unknown surface termination renders the origin of antiparallel interface coupling at YIG/FM interfaces impossible to determine theoretically. Instead, we provide additional insight experimentally using a suite of characterization techniques including polarized neutron reflectometry (PNR), x-ray photoemission electron microscopy (XPEEM), magnetometry, and x-ray diffraction (XRD). These techniques are applied to a range of heterostructures including YIG/Py grown on $\mathrm{Si/SiO_2}$ with and without a Pt seed layer, YIG/Py grown on (111) GGG and (110) GGG/Pt, and YIG/Co grown on $\mathrm{Si/SiO_2}$/Pt. This selection of samples allows for variation in ferromagnetic metal selection, film quality, crystallographic orientation, and surface termination. These results yield critical insights for the design and implementation of CMOS-compatible magnetic insulator/ferromagnetic metal hybrid structures for magnon logic.

II. METHODS

On (001)-oriented $\mathrm{Si/SiO_2}$ substrates, we studied a series of thin-film samples with nominal stack structures of Pt (0 nm or 10 nm)/YIG (35 nm)/Py or Co (20 nm)/Ru (3 nm) or Ta (5 nm) and YIG(30 nm)/Py(20 nm)/Ru(4 nm). We compare these samples to stacks grown on (110)-oriented GGG substrates with the structure Pt(10 nm)/YIG(35 nm)/Py(20 nm)/Ta(5 nm) and (111)-oriented GGG/YIG (50 nm)/Py(20 nm)/Ta(5 nm). The Pt and YIG are grown sequentially by ultrahigh-vacuum magnetron sputtering at room temperature, using an Ar sputtering pressure of 0.26 Pa (2 mTorr). The Pt layer was grown by dc magnetron sputtering, while the YIG was grown by rf sputtering. The $\mathrm{Si/SiO_2}$/Pt/YIG stacks are annealed at 850 °C for 3 min in a rapid thermal annealer with sufficient oxygen flow inside. The sample was returned to vacuum to deposit a metallic FM layer, and a Ru or Ta capping layer was deposited on top of the FM layer using dc magnetron sputtering with the same temperature and pressure as the initial layers.

The crystal structure was primarily probed through a combination of symmetric XRD scans along the growth axis and in-plane rotation scans of Bragg reflections with both in-plane and out-of-plane components. Because the XRD provided ambiguous results from the (110)-oriented GGG/Pt/YIG/Py samples, supplemental scanning transmission electron microscopy (STEM) and electron diffraction measurements were performed on this geometry. Cross-sectional specimens were prepared by focused ion-beam lift-out. Before lift-out, protective layers of sputtered carbon followed by ion-beam deposited Pt-C were applied to the surface of the thin film. Rough milling steps were performed with 30-keV Ga+ ions, and the final thinning of the sample was at 5 keV to reduce surface damage. High-resolution STEM experiments were then performed by a (S)TEM instrument operating with a primary beam energy of 300 keV. Annular dark-field images were acquired using a high-angle annual dark-field detector with a convergence semiangle of 13.7 mrad and inner collection semiangle of approximately 60 mrad. Nanobeam electron diffraction STEM measurements were performed with a convergence semiangle of 0.16 mrad and were collected with a 1-ms dwell time at (256 × 256) pixels per diffraction pattern with a bit depth of 12.

Magnetic properties are characterized by magnetometry measurements using a vibrating sample magnetometer (VSM) at room temperature, and the parallel (longitudinal, $M_{\parallel}$) and perpendicular (transverse, $M_{\perp}$) magnetization components were measured with the applied field in the plane of the film. First-order reversal curve (FORC) measurements [19–23] were also carried out using the same VSM in the longitudinal configuration: the sample was first saturated in a positive magnetic field of 300 mT; then, the magnetic field (H) was decreased to a given reversal field (H_R) and the magnetization, $M(H, H_R)$, was measured while the field was swept back to positive saturation. This process was repeated at successively more negative H_R, creating a family of FORCs. The normalized FORC distribution can then be calculated using the mixed second-order derivative of the magnetization $\rho(H_R, H) \equiv -\frac{1}{2M_s}\partial^2 M(H_R, H)/\partial H_R \partial H$. We have previously carried out detailed magnetometry on similar $\mathrm{Si/SiO_2}$/Pt/YIG/Py samples and found the saturation magnetizations of YIG and Py were in close agreement with the bulk.

Depth dependence of the nuclear structure and in-plane component of the magnetization were characterized using PNR. Data were collected using the Polarized Beam Reflectometer and Multi-Angle Grazing-Incidence K-vector instruments at the National Institute of Standards and Technology Center for Neutron Research. The incident neutrons were spin polarized parallel or antiparallel to the in-plane applied magnetic field (H), and reflectivity was measured with full polarization analysis ($R^{\uparrow\uparrow}$, $R^{\uparrow\downarrow}$, $R^{\downarrow\uparrow}$, $R^{\downarrow\downarrow}$, where arrows indicate the up- and down orientation of the incident and scattered neutron spin moment) as a function of the momentum transfer (Q_z) normal to the surface of the film. The nonspin-flip cross sections ($R^{\uparrow\uparrow}$, $R^{\downarrow\downarrow}$) are sensitive to the net magnetization component aligned with H and perpendicular with Q_z, whereas the spin-flip cross sections ($R^{\uparrow\downarrow}$, $R^{\downarrow\uparrow}$) probe the net magnetization perpendicular to both H and Q_z. PNR measurements were collected at room temperature with a maximum magnetic field of 700 mT applied along an in-plane direction of the sample. The magnetic field was first set to 700 mT and then progressively lowered for each field-state measurement. We reduced and model fit the PNR data using the REDUCTUS and REFL1D software packages, respectively [24,25]. Model fitting of the PNR data was carried out using a slab model, in which each layer is represented as a region of uniform nuclear and magnetic scattering length density with Gaussian interfacial roughness between adjacent layers; the model allowed for magnetic dead layers at the interfaces. For the case that a single sample was measured multiple times in different field states, the models were co-refined such that all data are fit to the same structural parameters, and only the magnetization varies with H.

To better understand the magnetic domain structure of the Py and Co layers with elemental specificity, we probed the FM layer using X-PEEM with spatially resolved x-ray absorption spectroscopy and x-ray magnetic circular dichroism (XMCD) at the Advanced Light Source PEEM-3 end station (beamline 11.0.1.1). Prior to image collection, an in-plane field of 650 mT was *ex situ* applied along the sample plane, and then lowered to zero. Data were collected at room temperature with x-ray illumination applied at a grazing incidence angle of 30 °, capturing predominantly the in-plane magnetization. Measurements were performed in zero field, as is necessary for full-field PEEM. Fe, Ni, and Co, $L_{2,3}$ absorption spectra were measured for the Si/SiO$_2$/Pt/YIG/Ru, Si/SiO$_2$/Pt/YIG/Py/Ru, and Si/SiO$_2$/Pt/YIG/Co/Ta samples, respectively, to determine the energy of maximum XMCD-based contrast for imaging (Fe 709.6 eV, Ni 853 eV, and Co 779 eV). The scans used to determine these energies are shown in the Supplemental Material, Figs. S9, S10, and S11 [26]. Magnetic contrast images were then obtained by measuring with alternating left- and right-circularly polarized light and taking the difference in intensity between the two polarization states at the XMCD maximum energy. Images taken at a pre-edge energy were used to normalize the magnetic contrast at each polarization. Vector maps of the magnetization magnitude and direction were obtained by pixelwise fitting of data collected at four different azimuthal angles (0 °, 45 °, 90 °, and 180 °). An additional Si/SiO$_2$/Pt/YIG/Ru sample was also imaged at five different azimuthal angles (0 °, 45 °, 90 °, 135 °, and 180 °) to understand the domain configuration of sputtered YIG when not in contact with a ferromagnetic metal.

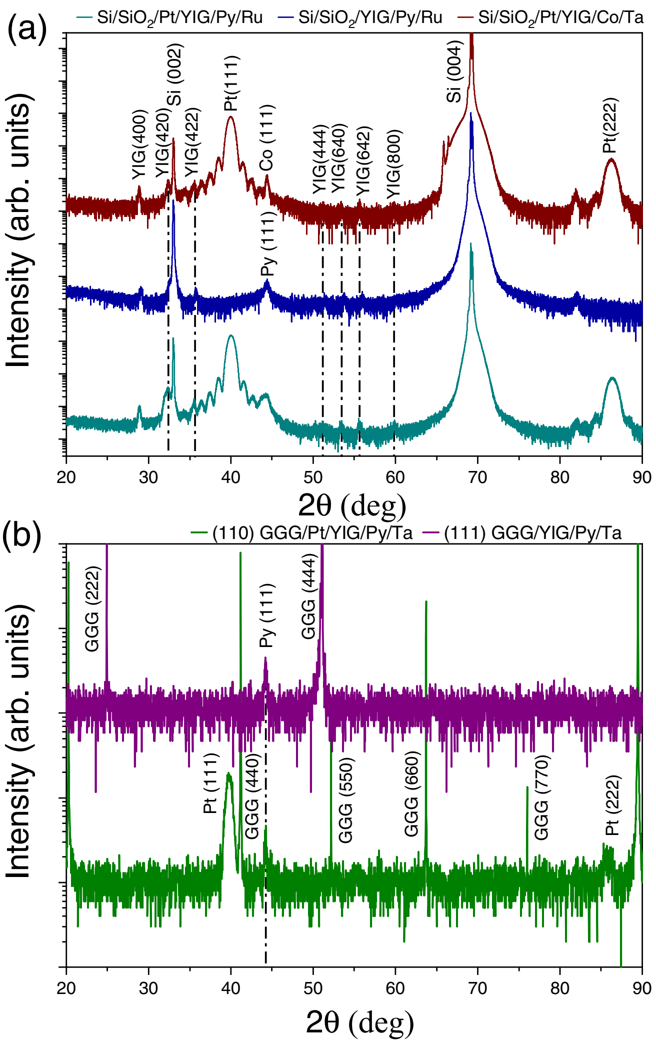

FIG. 1. (a) Si/SiO$_2$-based heterostructures for use of Py (teal) or Co (blue) as the ferromagnetic metal layer. Further, a sample with no Pt seed layer (maroon). (b) (110)-oriented GGG/Pt/YIG/Py/Ta and (111)-oriented GGG/YIG/Py/Ta. Dashed lines are intended to guide the eye for subtle peaks present across multiple samples.

III. RESULTS

The θ-2θ XRD scans on the YIG/Py and YIG/Co samples grown on Si/SiO$_2$ shown in Fig. 1 reveal a highly (111)-textured Pt seed layer and polycrystalline YIG with large (420) and (422) reflections alongside a number of secondary textures such as (400), (444), (640), and (642) along the Si [001] direction. Figure 1(a) also shows peaks consistent with (111) Py and (111) Co textures, respectively. To search for in-plane crystallographic ordering of the YIG, we rotated a sample about the film-normal direction while in the Bragg condition for the (642) plane of YIG and found no evidence of strong in-plane YIG texturing. No in-plane texturing was expected since the SiO$_2$ underlayer is presumed to be amorphous and no XRD peaks for the SiO$_2$ were observed. To assess the role of the Pt seed layer, Fig. 1(a) also shows an otherwise

TABLE I. Summary of the estimated volume fraction of various detected crystallographic orientations for the Si/SiO_2/Pt/YIG/Py/Ru, Si/SiO_2/Pt/YIG/Co/Ta, and Si/SiO_2/YIG/Py/Ru samples. Calculations based on theoretical intensities from the Inorganic Crystal Structure Database.

Orientation	SiO_2/Pt/YIG/Py/Ru vol. frac. (%)	SiO_2/Pt/YIG/Co/Ta vol. frac. (%)	SiO_2/YIG/Py/Ru vol. frac. (%)
400	4.5	9.0	8.3
420	61.9	29.1	23.4
422	18.4	37.9	22.1
444	2.0	0	10.2
640	3.6	7.8	13.8
642	9.7	16.2	22.2

identical sample without a Pt layer. While a shoulder persists in the YIG (420) position next to the Si (002) reflection, all YIG peaks are significantly weakened relative to the Pt-seeded samples.

Indeed, Table I shows the estimated volume fractions based on YIG integrated peak area and theoretical reflection intensity. There is considerable scatter in volume fraction from sample to sample, with the (420)-oriented fraction varying between 23 and 62%. The two samples grown with a Pt seed layer both exhibit (420) and (422) dominance, while the sample grown without Pt has comparable volume fractions of the (420)-, (422)-, and (642)-oriented YIG grains. We conclude, therefore, that the highly oriented Pt underlayer enhances the dominance of (420) and/or (422) texture in the YIG films in addition to improving YIG crystallinity. For relative crystallinity information, see Table SI in the Supplemental Material, which normalizes the YIG diffraction peak intensities to the Si (004) peak intensity of each scan and reveals significant suppression of all YIG diffraction peaks when samples are grown without a Pt layer.

Lastly, Fig. 1(b) shows XRD from (111)-oriented GGG/YIG/Py/Ta and (110)-oriented GGG/(111)-textured Pt/YIG/Py/Ta samples. Both stack structures were designed to present a (111)-oriented growing surface to maintain consistency with the (111)-oriented Pt grown on amorphous SiO_2. The (111)-oriented GGG/YIG represents the classic case of direct, high-quality epitaxial YIG growth, and the expected YIG film peaks and Pendellösung fringes may be observed for the sample on (111)-oriented GGG (see Supplemental Material, Fig. S1). On the other hand, (110)-oriented GGG/Pt should provide an intermediate growth between the extremes of epitaxy and amorphous SiO_2. Indeed, azimuthal φ scans of the asymmetric GGG (642) and Pt (311) peaks, plotted in Supplemental Material, Fig. S2, show that the GGG imparts a preferential in-plane orientation to the Pt. However, no obvious YIG Bragg reflections or Pendellösung fringes are observable in this sample, either from textures matching the underlying GGG or alternative crystallographic orientations. Because previous examples of this stack geometry have shown relatively close, but not perfect, alignment between the YIG and GGG, we performed STEM imaging and electron diffraction measurements on a (110)-oriented GGG/Pt/YIG/Pt heterostructure [27]. These measurements revealed that while the Pt interlayer does transmit preferred in-plane and out-of-plane orientations from the GGG to the YIG, there is approximately 2° tilt offset between the substrate and film (see Supplemental Material, Fig. S3). Such an offset renders the (110)-type YIG peaks extremely difficult to locate, as the angular offset is likely to vary in both magnitude and direction between domains, requiring extremely fine φ-ω (azimuthal and tilt offset) mapping to observe.

The room-temperature longitudinal and transverse hysteresis loops [28,29] are shown in Fig. 2 and Supplemental Material, Fig. S4, respectively, for the YIG/Py and YIG/Co samples on Si/SiO_2 [26,29–40]. For the YIG/Py sample, as the field is decreased from positive saturation at 300 mT, there is initially a gradual decrease in YIG longitudinal magnetization to achieve an antiparallel alignment between the YIG and the Py [Fig. 2(a)], as shown by previously reported PNR results [18]. Subsequently, application of a small negative field yields a sharp switching associated with the Py layer reversal, along with a coercivity of 0.7 mT; presumably the YIG also reverses, now pointing in a positive orientation, to maintain its antiparallel alignment [41]. Based on the magnetization and given the thicknesses and saturation moment determined previously [18], the YIG is not fully reversed at the coercive field and may contain domains,

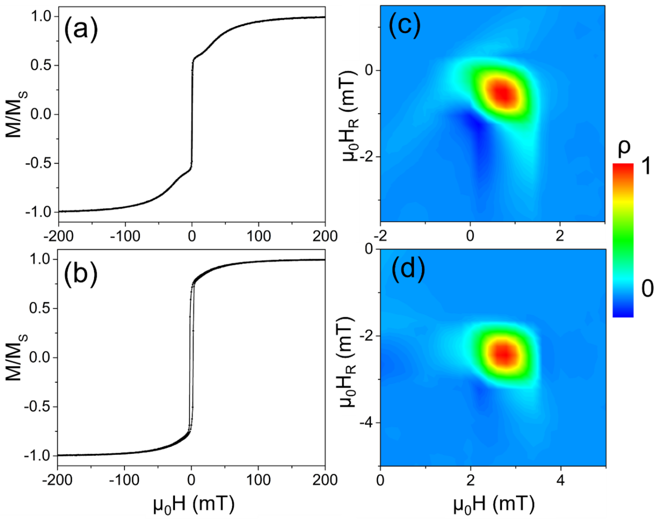

FIG. 2. (a), (b) In-plane longitudinal hysteresis loops and (c), (d) FORC distribution for (a), (c) Si/SiO_2/Pt/YIG/Py/Ru and (b), (d) Si/SiO_2/Pt/YIG/Co/Ta samples, respectively.

reducing the net magnetization. At more negative fields, the YIG is gradually forced into alignment with the applied field, although a very small slope persists through the entire measurement range. For the YIG/Co sample, the longitudinal moment exhibits a similar trend with magnetic field as the YIG/Py sample, except for differences in the loop shape and a relatively larger low-field switching component with an M/M_S of approximately 0.78 before switching [Fig. 2(b)].

FORC distributions for the YIG/Py and YIG/Co samples are shown in Figs. 2(c) and 2(d), displaying a single peak at ($\mu_0 H, \mu_0 H_R$) of (0.7, −0.5) mT and (2.7, −2.4) mT, respectively. The associated families of FORCs and full field-range FORC distributions are shown in Supplemental Material, Fig. S5 [26]. Interestingly, we find that the FORC distributions for both YIG/Py and YIG/Co samples to be featureless except near the soft layer switching fields. Reviewing the full-range FORC diagram, shown in the Supplemental Material, Fig. S5, the low-field features in Figs. 2(c) and 2(d) are the only nonzero contributions to the FORC diagram, indicating that the switching of the YIG layer at higher fields is mostly reversible [26]. The FORC features in Figs. 2(c) and 2(d) are associated with the irreversible Py or Co layer switching and indicate reversal by domain nucleation and propagation [38,42].

To directly probe the magnetization in the Si/SiO_2/Pt/YIG/FM heterostructures, we make use of PNR to measure the depth profile of the chemical composition and the net in-plane magnetization. A summary of our previously reported PNR data and model fitting of the Si/SiO_2/Pt/YIG/Py/Ru is presented in Ref. [18]. In that work, scattering-length density profiles corresponding to the best fits indicated parallel alignment of YIG and Py at magnetic fields above 150 mT. Below 150 mT, the YIG begins to reorient into an antiparallel configuration with respect to H and Py. Our previous PNR investigation of comparable-thickness Si/SiO_2/Pt/YIG/Py/Ru samples also revealed chemical compositions near theoretical bulk values, sharp interfaces, magnetic depth profiles in strong agreement with the magnetometry, and a lack of any statistically significant magnetic dead layer [18]. While spin-flip data were collected in this study, no statistically significant signals were observed after polarization correction, indicating the absence of a significant net in-plane magnetization perpendicular to the applied field.

To determine the generality of antiparallel coupling at YIG/FM interfaces for samples grown on Si/SiO_2, we probed a Si/SiO_2/Pt/YIG/Co/Ta heterostructure with PNR. The fitted non–spin-flip PNR cross sections from this sample at $\mu_0 H = 700$ mT, 4 mT, and 2 mT are shown in Fig. 3(a). Nonzero spin-flip scattering was observed at both 4 mT and 2 mT, and these cross sections are shown alongside theoretical fits in Fig. 3(b). To illustrate the relative scaling of the spin-flip and non–spin-flip signals, they are plotted on the same scale for the 4 mT condition in Fig. S7. The nonzero spin-flip measurements imply a net in-plane moment orthogonal to the guide field in the 4 mT and 2 mT measurements which, as discussed above, may be the result of subtle growth morphology effects which may occur even in films without in-plane texturing [43,44]. Low-field data were therefore fit using models which allowed the direction of the net in-plane moment in both the YIG and Co layers to independently rotate away from the applied field. The fitted spin asymmetry ($\mathrm{SA} = \frac{R^{++}-R^{--}}{R^{++}+R^{--}}$), which emphasizes the scattering contributions of the net magnetization parallel to the magnetic field, is plotted in Fig. 3(c). The scattering-length density profiles corresponding to the best fits to the data are shown in Fig. 3(d) and reveal sharp interfaces, nuclear and magnetic scattering-length densities in close agreement with expected values, and no magnetic dead layers at 700 mT apart from a small region at the top surface of the Co layer. Describing the low-field data required mostly antiparallel alignment of the YIG and Co moments, with angles of 161(2)° and 153(2)° between the YIG and Co moments at 2 mT and 4 mT, respectively; 180° denotes fully antiparallel in-plane alignment. The fitted YIG magnetization at 2 mT and 4 mT is 61(4)% and 58(3)% of the 700 mT saturated value, respectively, suggesting that the YIG likely forms partially canceling domains with a weak perpendicular component to the magnetization. This agrees with the previously reported behavior at the YIG/Py interface, in which approximately 76% of the moment is recovered in the antiparallel YIG at 4 mT. In contrast to the Py magnetization in Si/SiO_2/Pt/YIG/Py/Ru samples, the Co magnetization in Si/SiO_2/Pt/YIG/Co/Ta is found to rotate away from the applied field by as much as 10.55(5)° at low field; this rotation is proposed to be the result of an as-of-yet unidentified in-plane anisotropy. The magnetization data (Fig. S4) provide further evidence of this weak uniaxial anisotropy. Though the Co film has no net in-plane crystalline orientation, we speculate that microstructural details may be responsible for this effect [39,40,43].

We note that one feature in the PNR of Si/SiO_2/Pt/YIG/Co/Ta is extremely difficult to account for in the fitting. A splitting appears between the two non–spin-flip cross sections below the critical edge at low field. While a feature of this type is expected due to the large magnetic moment and slightly larger (relative to Fe or Ni) neutron absorption cross section of Co, the effect is too large to originate solely from these factors. Instead, we posit that domain formation driven by Co anisotropy leads to off-specular scattering which acts to preferentially remove intensity primarily from one of the non–spin-flip cross sections [33,45]. We confirm this hypothesis by performing a series of rocking curves on the sample at different Q_z values to identify the associated off-specular reflections. Some modifications in the standard data treatment are required to address these effects in the PNR analysis to account for this and are discussed in detail in the Supplemental Material [26].

We obtained a more detailed understanding of different domain structures in YIG/Py and YIG/Co grown on Si/SiO_2/Pt using magnetic domain imaging with X-PEEM. Figure 4 shows in-plane vector magnetometry maps obtained by using five XMCD PEEM images taken at 0°, 45°, 90°, 135°, and 180° to pixelwise fit the magnetization directions in each field of view in a bare YIG/Ru film, a YIG/Py/Ru film, and a YIG/Co/Ta film, all grown on Si/SiO_2/Pt. While three angles (e.g. 0°, 90°, and 180°) are sufficient to determine the three-dimensional magnetization orientation in the field of view, additional images at intermediate angles were used in the fitting for better statistical confidence in the pixelwise fits. Here we note that the images shown for YIG, YIG/Py, and

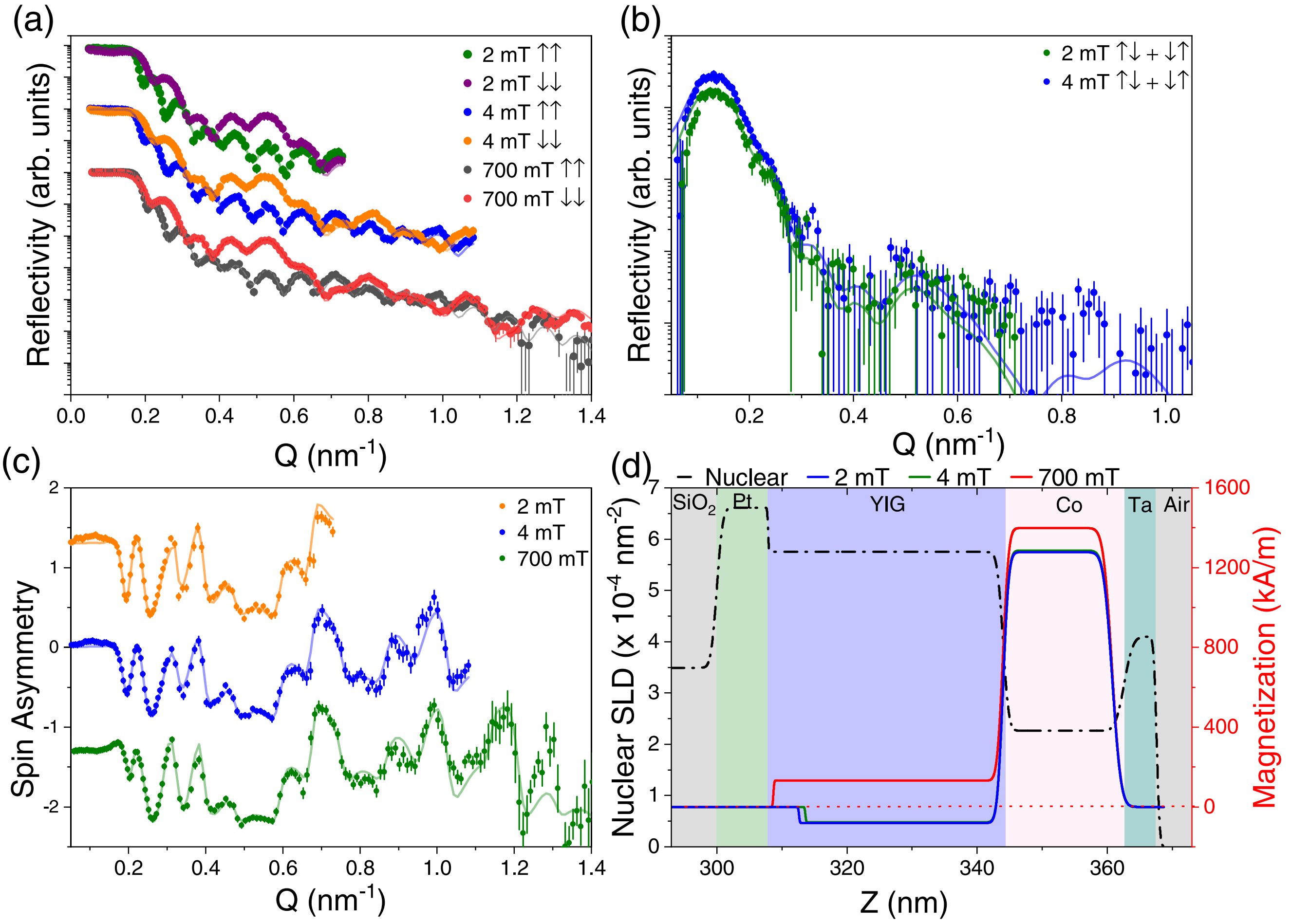

FIG. 3. (a) Non–spin-flip PNR data and theoretical fits for the Si/SiO$_2$/Pt/YIG/Co/Ta sample at 700 mT, 4 mT, and 2 mT. (b) Spin-flip reflectivities at 4 mT and 2 mT with theoretical fits. (c) Spin asymmetries and fits at 700 mT, 4 mT, and 2 mT. (d) Nuclear and magnetic depth profiles used to generate the fits shown. Note that the low-field canting angles of the magnetization discussed in the text are not shown. Error bars indicate single standard deviation uncertainties based on counting statistics.

YIG/Co were taken using the Fe, Ni, and Co L_3 edges as described in Methods and Supplemental Material [26]. The $L_{2,3}$ absorption spectra for Co on the YIG/Co sample, and Fe and Ni on the YIG and YIG/Py samples, respectively, are shown in Supplemental Material, Figs. S9, S10, and S11, respectively [26], and indicate no significant oxidation of the surface Co or Py [46]. The thicknesses of the Py and Co layers were well beyond the photoelectron escape depth of approximately 5 nm, so that it was not possible to image the underlying YIG, and we instead use a bare YIG film for comparison. Further, it is critical to recall the extremely weak anisotropy of Py. Since the PNR measurements required a magnetic field of at least 1 mT to maintain neutron polarization while the X-PEEM must be done in zero field, the domain state of the Py (and consequently the underlying YIG) may be very different for the PNR and X-PEEM measurements. That being said, the PEEM data confirm the PNR observation that the Py and Co layers dominate the magnetization, aligning mostly parallel to the initializing field at remanence.

Nevertheless, key insights may be gleaned by comparing the images in Fig. 4. Specifically, the YIG and Py domains appear to have very similar morphology, indicating that the YIG domain structure is being imprinted onto the permalloy, with domains approximately 2 μm to 5 μm in their lateral dimensions. These images also show that the YIG and YIG/Py samples have no significant asymmetry in the reversal directions. In contrast to the lack of a preferred direction in the Py, the Co image shows a significantly different magnetic domain structure, with widths parallel to the conditioning field of approximately 5 μm, but lengths orthogonal to the field of > 20 μm. This domain structure is consistent with a uniaxial anisotropy induced in Co through microstructural effects induced by the growth morphology, emphasizing that while the coupling across the interface is similar across different FM systems, the low-field behavior may be tuned by varying materials choice and growth parameters [39,40,43].

Having demonstrated that the antiparallel alignment of the YIG and FM layers at low field appears to be a generalizable behavior in Si/SiO$_2$/Pt/YIG/FM structures, we may better understand the fundamental underpinnings by turning our attention to alternative structures. We performed PNR at 700 mT and 4 mT on a Si/SiO$_2$/YIG/Py/Ru structure in which the YIG is grown without a Pt seed layer. The 4 mT measurement and the associated best-fit depth profile are shown in Fig. 5. Once again, we find high-quality interfaces, bulklike scattering-length densities, and antiparallel alignment of the

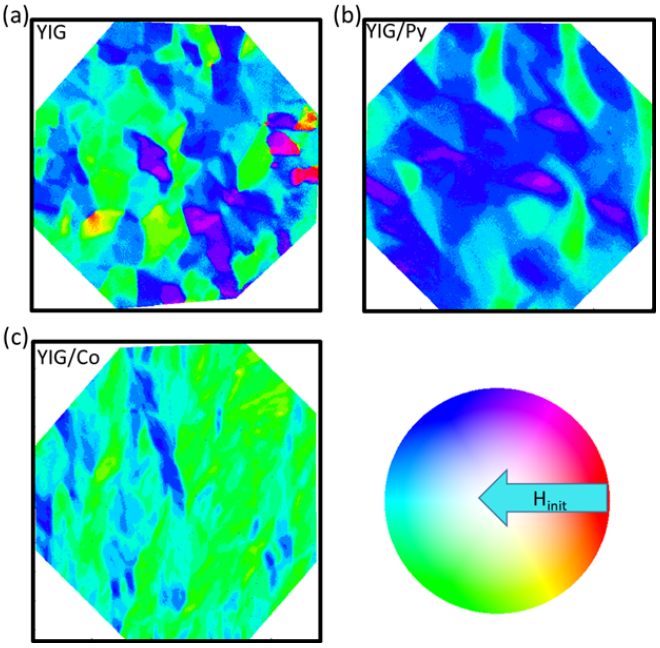

FIG. 4. In-plane magnetic moment orientation determined from XMCD-PEEM data at the L_3 edge of (a) Fe on the Si/SiO$_2$/Pt/YIG/Ru, (b) Ni on the Si/SiO$_2$/Pt/YIG/Py/Ru sample, and (c) Co on the Si/SiO$_2$/Pt/YIG/Co/Ta sample. The field of view for all images is 28 μm. (d) Color mapping of the in-plane moment angle in (a), (b), and (c).

YIG and Py. The lack of a Pt seed layer appears to suppress the magnetization in the YIG layer, likely as a result of the reduced crystallinity revealed by the x-ray diffraction of Fig. 1. Nevertheless, approximately 80% of the saturated YIG magnetization appears to be aligned antiparallel at 4 mT in this sample, suggesting that it is not the YIG crystal quality which determines the sign of the interface exchange coupling.

Since crystal quality appeared not to be the decisive factor in the observed antiferromagnetic coupling, we also probed the role of crystallographic orientation by measuring PNR on a pair of YIG/Py samples grown on GGG with and without a Pt seed layer. In Fig. 6, we show the measured PNR, model fits, and spin asymmetry for both of these samples, which had nominal structures of (110) GGG /Pt (10 nm)/YIG (35 nm)/Py (20 nm)/Ta (5 nm) and (111) GGG/YIG (50 nm)/Py (20 nm)/Ta (5 nm), measured at 700 mT and 0.9 mT. In both cases, we find only minor changes in the magnetic depth profile between high- and low-field measurements, and a clear absence of the antiparallel coupling that is seen in the Si/SiO$_2$-based samples. This conclusion is reinforced by the near-perfect overlap of the spin asymmetry at both field conditions (see Fig. S8 in the Supplemental Material) [26]. While this result is well reported in the literature, it remains quite interesting in that it highlights that exchange coupling between YIG and well-known ferromagnetic metals is tied to the sample design in a nontrivial way.

Of further interest is the resulting magnetic depth profiles near the (111) GGG/YIG and (110) GGG/Pt/YIG interfaces in the two samples. While the (111) GGG/YIG sample exhibits a room-temperature magnetic dead layer in the first few nanometers of the YIG layer, this feature is absent in the GGG/Pt/YIG, despite a lower-density transitional growth region in the latter sample. The dead layer observed at the direct GGG/YIG interface is consistent with varying reports of a structural and magnetic reconfiguration associated with interdiffusion in the relatively open garnet structures [16,17,47]. We speculate that the Pt may act as an effective diffusion barrier while simultaneously preserving a highly oriented crystal structure on which to grow high-quality YIG.

IV. DISCUSSION

In the Introduction, we posited that a complex interplay of many factors was likely to play a role in determining the sign of interface coupling at the YIG/FM interface. Specifically, we identified surface termination, FM choice, structural disorder, and deposition technique selection as potential factors. In this work, we narrowed the range of possible explanations through the application of XRD, magnetometry, PNR, XPEEM, and STEM to a range of sample designs, summarized in Table II, that provides a more comprehensive understanding of interfacial magnetic coupling in YIG/FM heterostructures.

We show that the antiparallel interface coupling is preserved when substituting Co for Py, leading us to suspect that the antiparallel coupling results from direct transition metal to ferromagnetic metal exchange at the interface rather than a very specific superexchange interaction unique to YIG/Py. Further, we found that the antiparallel exchange coupling is preserved in samples with sharply reduced YIG crystallinity for samples grown on SiO$_2$ without a Pt seed layer. In contrast, any growth stack resulting in a highly in-plane oriented or epitaxial YIG film coupled ferromagnetically across the interface. This is true for YIG grown on both (111) GGG, where the YIG matches the underlying orientation of the substrate, and (110) GGG/Pt, where the YIG is relatively (110)-oriented albeit with some tilt misalignment and lower crystal quality. This combination of observations tends to rule out FM choice, disorder, and deposition-specific issues while implicating the surface termination of the YIG films.

However, the observations of Klingler *et al.* remain challenging to reconcile. Specifically, while our high-quality (111) GGG/(111) YIG/FM layers support ferromagnetic YIG-FM exchange, the (111)-GGG/YIG/Co in Klingler *et al.* shows indications of some form of antiparallel alignment [8]. We speculate that the surface terminations of these two samples may be very different, as Klingler *et al.* follow a YIG surface preparation approach from Pütter *et al.* which is known to alter the relative surface concentrations of Y, Fe, and O in favor of relatively higher Y and O concentrations [48]. These observations are, therefore, consistent with a picture of YIG/FM interface coupling which is highly sensitive to the interface configuration.

Having identified the likely source of anomalous magnetic coupling in the system, we find several likely candidate textures. YIG layers grown on amorphous SiO$_2$ exhibit primarily (420), (422), and (642) orientations with or without a Pt seed layer [27]. Some weaker textures observable in these samples include the (400), (444), and (640), but for samples with a Pt

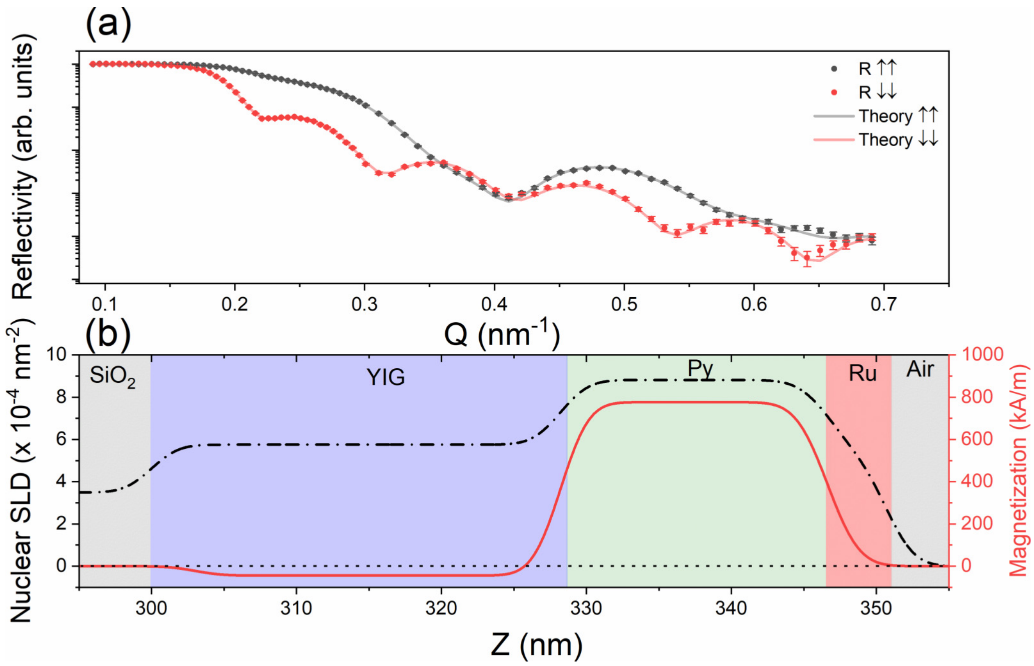

FIG. 5. (a) Non–spin-flip PNR data and theoretical fits for a Si/SiO$_2$/YIG/Py/Ru sample at 4 mT. (b) Non–spin-flip reflectivities at 4 mT and with theoretical fits. (b) Nuclear (black, dashed-dotted, left axis) and magnetic (red, solid, right axis) depth profiles used to generate the fits shown. Error bars indicate single standard deviation uncertainties based on counting statistics.

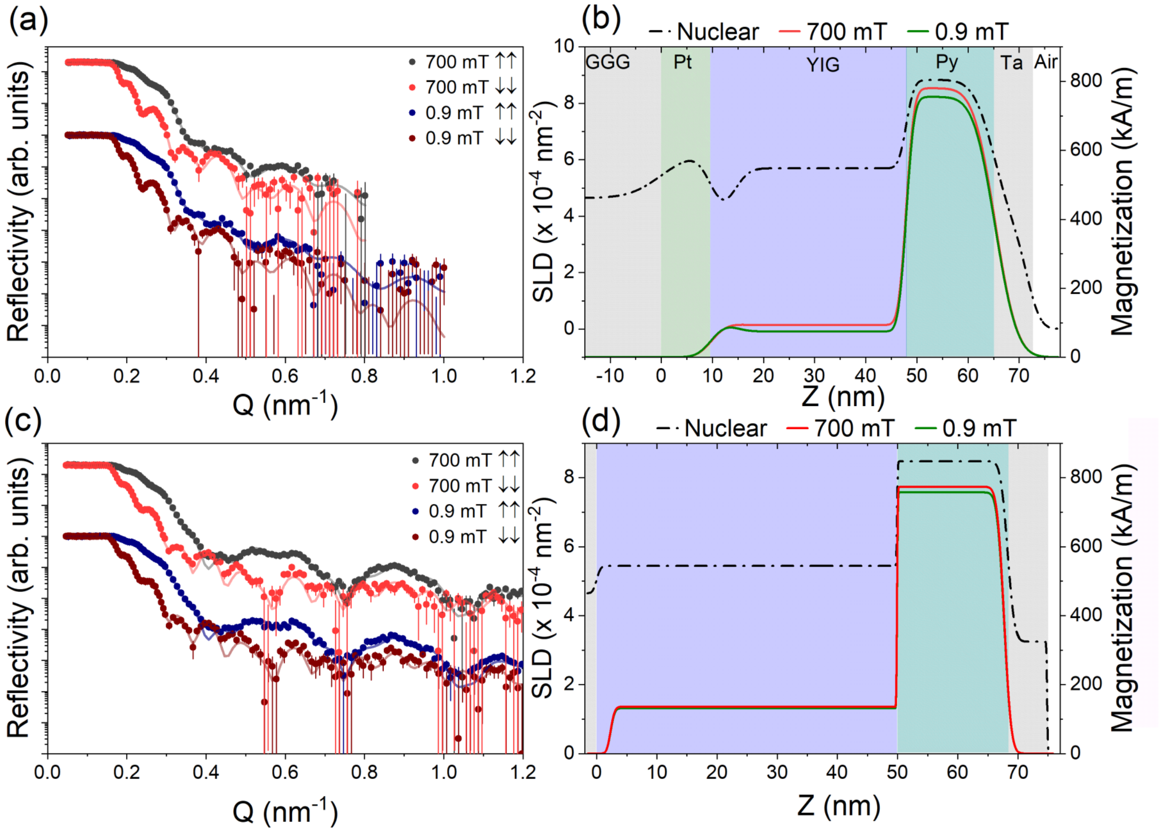

FIG. 6. (a) PNR data and model fits for (110) GGG/Pt(10 nm)/YIG(35 nm)/Py(20 nm)/Ta(5 nm) collected at 700 mT and 0.9 mT. (b) Nuclear scattering-length density profiles (left axis, dashed-dotted) and magnetization depth profile (right axis, solid) obtained from model fitting the PNR data in (a). (c) PNR data and model fits for (111) GGG/YIG(50 nm)/Py(20 nm)/Ta(5 nm) with associated depth profiles in (d). Note that $Z = 0$ nm refers to the surface of the GGG substrate. Error bars indicate single standard deviation uncertainties based on counting statistics.

TABLE II. Summary of sample geometries and the resulting orientations, magnetic couplings, and anisotropy observed.

Sample	YIG orientation	Coupling	Anisotropy
$Si/SiO_2/Pt/YIG/Co/Ta$	Textured	Antiferromagnetic	Strong
$Si/SiO_2/Pt/YIG/Py/Ru$ [18]	Textured	Antiferromagnetic	Weak
$Si/SiO_2/YIG/Py/Ru$	Polycrystalline	Antiferromagnetic	Weak
(111) GGG/YIG/Py/Ta	(111)	Ferromagnetic	Weak
(110) GGG/Pt/YIG/Py/Ta	(110)	Ferromagnetic	Weak

seed the volume fraction of these is sufficiently low that they are unlikely to contribute significantly to the exchange. We regard the (420) and (422) orientations as the most likely origins of the antiparallel coupling, given that these textures have consistently high volume fractions across all samples. The coexistence of many grain boundaries and different orientations on the YIG surface may also give rise to frustration and surface reconstruction, and the role of these effects is challenging to separate. Indeed, the details of the surface morphology and termination can lead to antiparallel exchange coupling even in highly oriented garnet films, as recently reported for $Tm_3Fe_5O_{12}$/W interfaces [49]. Given the surface sensitivity of the interfacial exchange coupling, either surface termination effects or microstructure-induced frustration remain plausible explanations and further work is required.

Lastly, we note differences in the reversal behavior of Co and Py, which indicate that anisotropy plays a role in the low-field configuration at the YIG/Co interface. As explored above, this anisotropy is unexpected in samples grown without significant in-plane texture, but Co anisotropy has been demonstrated in similar systems and is typically attributed to the specifics of the growth-dependent microstructure [39,40,43]. While we expect such behavior to vary considerably depending on the specific growth conditions used, it does represent an additional tuning parameter for use in the design of hybrid YIG/FM heterostructures for magnon spintronics. Specifically, the differences in anisotropy appear to lead to pronounced contrasts in the in-plane domain structure at low fields as determined by PEEM and verified by low-Q PNR features. While the YIG domain structure appears to imprint on an adjacent Py layer, this is not true of the Co, where a fine-structured uniaxial domain pattern emerges instead.

V. CONCLUSIONS

In summary, we have carried out detailed characterization and analysis of the coupling and switching methods in Si and GGG-based YIG/FM hybrid structures. The antiparallel coupling between YIG and ferromagnetic metals is confirmed for both Py and Co on films grown on $Si/SiO_2/Pt$. We further show that this preferential antiferromagnetic coupling is independent of the presence of a Pt seed layer for YIG growth and that the antiparallel coupling may be related to either certain dominant YIG film textures or the presence of disorder/grain boundaries at the YIG surface. Finally, we find that the antiparallel coupling does not manifest in analogous but highly oriented samples grown on (111) GGG and (110) GGG/Pt substrates with or without a Pt seed layer. These results implicate the termination surface in the YIG as the origin of the antiparallel mechanism. Lastly, we note that subtle differences were observed in the evolution of the low-field domain structure, including an in-plane anisotropy which dominates the Co orientation at low fields, which provides another potential knob through which to control the efficiency of magnon spin-valve efficiencies in garnet/metallic ferromagnet heterostructures.

ACKNOWLEDGMENTS

Research was performed in part at the National Institute of Standards and Technology (NIST) Center for Nanoscale Science and Technology. This research was partially supported by National Science Foundation, through the Massachusetts Institute of Technology Materials Research Science and Engineering Center (Grant No. DMR–1419807) and at Georgetown University (Grants No. ECCS-1933527 and No. ECCS-2151809), and by SMART, one of seven centers of nCORE, a Semiconductor Research Corporation program, sponsored by NIST. D.A.G. is partly supported by the DOE office of Basic Research, Award No. DE-SC0021344 This research used resources of the Advanced Light Source, which is a DOE Office of Science User Facility under Contract No. DE-AC02-05CH11231.

---

[1] Y. Kajiwara, K. Harii, S. Takahashi, J. Ohe, K. Uchida, M. Mizuguchi, H. Umezawa, H. Kawai, K. Ando, K. Takanashi, S. Maekawa, and E. Saitoh, Transmission of electrical signals by spin-wave interconversion in a magnetic insulator, Nature (London) **464**, 262 (2010).

[2] M. Wu and A. J. Hoffman, *Recent Advances in Magnetic Insulators: From Spintronics to Microwave Applications* (Academic Press, Cambridge, MA, 2013).

[3] L. J. Cornelissen, J. Liu, R. A. Duine, J. ben Youssef, and B. J. van Wees, Long-distance transport of magnon spin information in a magnetic insulator at room temperature, Nat. Phys. **11**, 1022 (2015).

[4] B. L. Giles, Z. Yang, J. S. Jamison, and R. C. Myers, Long-range pure magnon spin diffusion observed in a nonlocal spin-Seebeck geometry, Phys. Rev. B **92**, 224415 (2015).

[5] W. Jiang, P. Upadhyaya, Y. Fan, J. Zhao, M. Wang, L.-T. Chang, M. Lang, K. L. Wong, M. Lewis, Y.-T. Lin, J. Tang, S. Cherepov, X. Zhou, Y. Tserkovnyak, R. N. Schwartz, and K. L. Wang, Direct Imaging of Thermally Driven Domain Wall

Motion in Magnetic Insulators, Phys. Rev. Lett. **110**, 177202 (2013).

[6] A. V. Chumak, V. I. Vasyuchka, A. A. Serga, and B. Hillebrands, Magnon spintronics, Nat. Phys. **11**, 453 (2015).

[7] H. Yu, J. Xiao, and P. Pirro, Magnon spintronics, J. Magn. Magn. Mater. **450**, 1 (2018).

[8] S. Klingler, V. Amin, S. Geprägs, K. Ganzhorn, H. Maier-Flaig, M. Althammer, H. Huebl, R. Gross, R. D. McMichael, M. D. Stiles, S. T. B. Goennenwein, and M. Weiler, Spin-Torque Excitation of Perpendicular Standing Spin Waves in Coupled YIG/Co Heterostructures, Phys. Rev. Lett. **120**, 127201 (2018).

[9] J. Chen, C. Liu, T. Liu, Y. Xiao, K. Xia, G. E. W. Bauer, M. Wu, and H. Yu, Strong Interlayer Magnon-Magnon Coupling in Magnetic Metal-Insulator Hybrid Nanostructures, Phys. Rev. Lett. **120**, 217202 (2018).

[10] H. Qin, S. J. Hämäläinen, and S. van Dijken, Exchange-torque-induced excitation of perpendicular standing spin waves in nanometer-thick YIG films, Sci. Rep. **8**, 5755 (2018).

[11] E. Lee-Wong, R. Xue, F. Ye, A. Kreisel, T. van der Sar, A. Yacoby, and C. R. Du, Nanoscale detection of magnon excitations with variable wavevectors through a quantum spin sensor, Nano Lett. **20**, 3284 (2020).

[12] Z. Zhang, M. O. Scully, and G. S. Agarwal, Quantum entanglement between two magnon modes via Kerr nonlinearity driven far from equilibrium, Phys. Rev. Res. **1**, 023021 (2019).

[13] R. G. E. Morris, A. F. van Loo, S. Kosen, and A. D. Karenowska, Strong coupling of magnons in a YIG sphere to photons in a planar superconducting resonator in the quantum limit, Sci. Rep. **7**, 11511 (2017).

[14] H. Wu, L. Huang, C. Fang, B. S. Yang, C. H. Wan, G. Q. Yu, J. F. Feng, H. X. Wei, and X. F. Han, Magnon Valve Effect between Two Magnetic Insulators, Phys. Rev. Lett. **120**, 097205 (2018).

[15] J. Cramer, F. Fuhrmann, U. Ritzmann, V. Gall, T. Niizeki, R. Ramos, Z. Qiu, D. Hou, T. Kikkawa, J. Sinova, U. Nowak, E. Saitoh, and M. Kläui, Magnon detection using a ferroic collinear multilayer spin valve, Nat. Commun. **9**, 1089 (2018).

[16] A. Mitra, O. Cespedes, Q. Ramasse, M. Ali, S. Marmion, M. Ward, R. M. D. Brydson, C. J. Kinane, J. F. K. Cooper, S. Langridge, and B. J. Hickey, Interfacial origin of the magnetisation suppression of thin film yttrium iron garnet, Sci. Rep. **7**, 11774 (2017).

[17] S. M. Suturin, A. M. Korovin, V. E. Bursian, L. V. Lutsev, V. Bourobina, N. L. Yakovlev, M. Montecchi, L. Pasquali, V. Ukleev, A. Vorobiev, A. Devishvili, and N. S. Sokolov, Role of gallium diffusion in the formation of a magnetically dead layer at the $Y_3Fe_5O_{12}/Gd_3Ga_5O_{12}$ epitaxial interface, Phys. Rev. Mater. **2**, 104404 (2018).

[18] Y. Fan, P. Quarterman, J. Finley, J. Han, P. Zhang, J. T. Hou, M. D. Stiles, A. J. Grutter, and L. Liu, Manipulation of Coupling and Magnon Transport in Magnetic Metal-Insulator Hybrid Structures, Phys. Rev. Appl. **13**, 061002 (2020).

[19] E. C. Burks, D. A. Gilbert, P. D. Murray, C. Flores, T. E. Felter, S. Charnvanichborikarn, S. O. Kucheyev, J. D. Colvin, G. Yin, and K. Liu, 3D nanomagnetism in low density interconnected nanowire networks, Nano Lett. **21**, 716 (2021).

[20] M. T. Rahman, R. K. Dumas, N. Eibagi, N. N. Shams, Y.-C. Wu, K. Liu, and C.-H. Lai, Controlling magnetization reversal in Co/Pt nanostructures with perpendicular anisotropy, Appl. Phys. Lett. **94**, 042507 (2009).

[21] J. E. Davies, O. Hellwig, E. E. Fullerton, G. Denbeaux, J. B. Kortright, and K. Liu, Magnetization reversal of CoPt multilayers: Microscopic origin of high-field magnetic irreversibility, Phys. Rev. B **70**, 224434 (2004).

[22] C. R. Pike, A. P. Roberts, and K. L. Verosub, Characterizing interactions in fine magnetic particle systems using first order reversal curves, J. Appl. Phys. **85**, 6660 (1999).

[23] D. A. Gilbert, G. T. Zimanyi, R. K. Dumas, M. Winklhofer, A. Gomez, N. Eibagi, J. L. Vicent, and K. Liu, Quantitative decoding of interactions in tunable nanomagnet arrays using first order reversal curves, Sci. Rep. **4**, 4204 (2014).

[24] B. J. Kirby, P. A. Kienzle, B. B. Maranville, N. F. Berk, J. Krycka, F. Heinrich, and C. F. Majkrzak, Phase-sensitive specular neutron reflectometry for imaging the nanometer scale composition depth profile of thin-film materials, Curr. Opin. Colloid Interface Sci. **17**, 44 (2012).

[25] B. Maranville, W. Ratcliff II, and P. Kienzle, reductus*:* A stateless Python data reduction service with a browser front end, J. Appl. Crystallogr. **51**, 1500 (2018).

[26] See Supplemental Material at http://link.aps.org/supplemental/10.1103/PhysRevMaterials.6.094418 for additional details on x-ray diffraction, electron microscopy, vector magnetometry, and first-order reversal-curve measurements, as well as an expanded analysis of the polarized neutron reflectometry data and background x-ray photoemission electron microscopy data.

[27] Y. Fan, J. Finley, J. Han, M. E. Holtz, P. Quarterman, P. Zhang, T. S. Safi, J. T. Hou, A. J. Grutter, and L. Liu, Resonant spin transmission mediated by magnons in a magnetic insulator multilayer structure, Adv. Mater. **33**, 2008555 (2021).

[28] J. Olamit, K. Liu, Z.-P. Li, and I. K. Schuller, Irreversibility of magnetization rotation in exchange biased Fe/Epitaxial-FeF_2 thin films, Appl. Phys. Lett. **90**, 032510 (2007).

[29] J. E. Davies, O. Hellwig, E. E. Fullerton, J. S. Jiang, S. D. Bader, G. T. Zimányi, and K. Liu, Anisotropy dependence of irreversible switching in Fe/SmCo and FeNi/FePt exchange spring magnet films, Appl. Phys. Lett. **86**, 262503 (2005).

[30] Yu. N. Khaydukov, D. Lenk, V. Zdravkov, R. Morari, T. Keller, A. S. Sidorenko, L. R. Tagirov, R. Tidecks, S. Horn, and B. Keimer, Chirality of Bloch domain walls in exchange-biased CoO/Co bilayer studied by waveguide-enhanced neutron spin-flip scattering, Phys. Rev. B **104**, 174445 (2021).

[31] H. Zhang, P. D. Gallagher, S. K. Satija, R. M. Lindstrom, R. L. Paul, T. P. Russell, P. Lambooy, and E. J. Kramer, Grazing Incidence Prompt Gamma Emissions and Resonance-Enhanced Neutron Standing Waves in a Thin Film, Phys. Rev. Lett. **72**, 3044 (1994).

[32] T. Saerbeck, H. Huckfeldt, B. P. Toperverg, and A. Ehresmann, Magnetic structure of ion-beam imprinted stripe domains determined by neutron scattering, Nanomaterials **10**, 752 (2020).

[33] F. Radu, V. Leiner, K. Westerholt, H. Zabel, J. McCord, A. Vorobiev, J. Major, D. Jullien, H. Humblot, and F. Tasset, Magnetic induction and domain walls in magnetic thin films at remanence, J. Phys.: Condens. Matter **17**, 1711 (2005).

[34] E. Kentzinger, U. Rücker, B. Toperverg, F. Ott, and T. Brückel, Depth-resolved investigation of the lateral magnetic correlations in a gradient nanocrystalline multilayer, Phys. Rev. B **77**, 104435 (2008).

[35] S. P. Pogossian, A. Menelle, H. Le Gall, J. M. Desvignes, and M. Artinian, Experimental observation of guided polarized

neutrons in magnetic-thin-film waveguides, Phys. Rev. B **53**, 14359 (1996).

[36] S. V. Kozhevnikov, F. Ott, A. Paul, and L. Rosta, Resonances and off-specular scattering in neutron waveguides, Eur. Phys. J. Spec. Top. **167**, 87 (2009).

[37] Yu. Khaydukov, A. M. Petrzhik, I. v. Borisenko, A. Kalabukhov, D. Winkler, T. Keller, G. A. Ovsyannikov, and B. Keimer, Magnetic waveguides for neutron reflectometry, Phys. Rev. B **96**, 165414 (2017).

[38] J. Olamit and K. Liu, Rotational hysteresis of the exchange anisotropy direction in Co/FeMn thin films, J. Appl. Phys. **101**, 09E508 (2007).

[39] M. Z. Xue, S. L. Ding, R. Wu, L. Zha, G. Y. Qiao, H. L. Du, J. Z. Han, Y. C. Yang, C. S. Wang, and J. B. Yang, Thickness induced uniaxial anisotropy and unexpected four-fold symmetry in $\mathrm{Co/SiO_2/Si}$ films, AIP Adv **8**, 056311 (2018).

[40] T. Kuschel, T. Becker, D. Bruns, M. Suendorf, F. Bertram, P. Fumagalli, and J. Wollschläger, Uniaxial magnetic anisotropy for thin Co films on glass studied by magnetooptic Kerr effect, J. Appl. Phys. **109**, 093907 (2011).

[41] D. A. Gilbert, J. Olamit, R. K. Dumas, B. J. Kirby, A. J. Grutter, B. B. Maranville, E. Arenholz, J. A. Borchers, and K. Liu, Controllable positive exchange bias via redox-driven oxygen migration, Nat. Commun. **7**, 11050 (2016).

[42] D. A. Gilbert, P. D. Murray, J. de Rojas, R. K. Dumas, J. E. Davies, and K. Liu, Reconstructing phase-resolved hysteresis loops from first-order reversal curves, Sci. Rep. **11**, 4018 (2021).

[43] E. B. Park, S.-U. Jang, J.-H. Kim, and S.-J. Kwon, Induced magnetic anisotropy and strain in permalloy films deposited under magnetic field, Thin Solid Films **520**, 5981 (2012).

[44] J. Trastoy, A. Camjayi, J. del Valle, Y. Kalcheim, J.-P. Crocombette, D. A. Gilbert, J. A. Borchers, J. E. Villegas, D. Ravelosona, M. J. Rozenberg, and I. K. Schuller, Magnetic field frustration of the metal-insulator transition in V_2O_3, Phys. Rev. B **101**, 245109 (2020).

[45] H. J. Lauter, V. Lauter-Pasyuk, B. P. Toperverg, L. Romashev, V. Ustinov, E. Kravtsov, A. Vorobiev, O. Nikonov, and J. Major, Spin-resolved unpolarized neutron off-specular scattering for magnetic multilayer studies, Appl. Phys. A: Mater. Sci. Process. **74**, s1557 (2002).

[46] T. J. Regan, H. Ohldag, C. Stamm, F. Nolting, J. Lüning, J. Stöhr, and R. L. White, Chemical effects at metal/oxide interfaces studied by x-ray-absorption spectroscopy, Phys. Rev. B **64**, 214422 (2001).

[47] J. F. K. Cooper, C. J. Kinane, S. Langridge, M. Ali, B. J. Hickey, T. Niizeki, K. Uchida, E. Saitoh, H. Ambaye, and A. Glavic, Unexpected structural and magnetic depth dependence of YIG thin films, Phys. Rev. B **96**, 104404 (2017).

[48] S. Pütter, S. Geprägs, R. Schlitz, M. Althammer, A. Erb, R. Gross, and S. T. B. Goennenwein, Impact of the interface quality of Pt/YIG(111) hybrids on their spin Hall magnetoresistance, Appl. Phys. Lett. **110**, 012403 (2017).

[49] Q. Shao, A. Grutter, Y. Liu, G. Yu, C.-Y. Yang, D. A. Gilbert, E. Arenholz, P. Shafer, X. Che, C. Tang, M. Aldosary, A. Navabi, Q. L. He, B. J. Kirby, J. Shi, and K. L. Wang, Exploring interfacial exchange coupling and sublattice effect in heavy metal/ferrimagnetic insulator heterostructures using Hall measurements, x-ray magnetic circular dichroism, and neutron reflectometry, Phys. Rev. B **99**, 104401 (2019).